Engineering and Technology Journal

Promote Osseointegration Through Surface Functionalization of Ti-Zr Alloy by Nano Composite Fiber

Amjed Al-khateeb[a]*, **Emad S. Al-Hassani** [a] , **Akram R. Jabur** [a] , **Suriani Binti Abu Bakar** [b]

[a] Materials Engineering Dept., University of Technology-Iraq, Alsina'a street, 10066 Baghdad, Iraq.
[b] Departement of Physics., Nanotechnology Research Centre, Faculty of Science and Mathematics, Universiti Pendidikan Sultan Idris, 35900 Tanjung Malim, Perak, Malaysia.
*Corresponding author Email: mae.19.07@grad.uotechnology.edu.iq

HIGHLIGHTS

- Bio-metallic Ti-25Zr sample was prepared using powder metallurgy.
- Ti-25Zr alloy was coated using an electrospinning method to form a Nano-composite coating film.
- The coated sample significantly improves cell activity and resists bacterial infection.

ARTICLE INFO

ABSTRACT

Using bioactive and biocompatible coatings to biofunctionalized metallic implant surfaces for enhanced bone regeneration while resisting bacterial infection has attracted materials scientists' interest. Bio-metallic Ti-25Zr disc sample was prepared using powder metallurgy and then coated using an electrospinning method to form a nanocomposite fiber as a coating layer over the surface of the metal alloy substrate. Three nano-compounds (Nano-hydroxyapatite, Nano-Titanium dioxide, Nano-strontium titanite) were added individually to the Polycaprolactone/Chitosan blend to prepare the electrospinning solutions. The results show a significant improvement in biocompatibility for the coated samples after seven days of (MC3T3-E1) cell culture. Cell viability percentages were significantly higher for the coated samples compared to uncoated ones, with values of PCL/Chitosan/nHA (HA1) has 239.45±17.95%, PCL/Chitosan/nSrTiO$_3$ (SR1) has170.09±8.12%, and PCL/Chitosan/nTiO$_2$ (TI1) has 117.19±19.42%, while bare Ti-25Zr has 80.52±1.97%. Cell proliferation also shows a remarkable increase with time for coated samples, and the enhancement reaches 197.76% for (HA1), 111.38% (SR1), and 45.81 % (TI1) in comparison with (bare Ti-25Zr). For the antibacterial test, no inhibition zone for the control sample (bare Ti-25Zr) was observed, while the coated samples showed a suitable and comparable inhibition zone. The coating procedure is simple and inexpensive, and composite nano-fiber has high biocompatibility and promise in orthodontic and orthopedic bone regeneration.

1. Introduction

The surface is the first contact line and the implant's most crucial part. The biofunctionalization of implant surfaces using biocompatible and bioactive coatings for improved bone regeneration is a hot topic. The clinical requirement for prostheses that are effective against bacterial infections and promote osseointegration is increasing [1,2].

Because of their excellent biocompatibility, corrosion resistance, high strength, and low density, Ti-alloys implants are the most commonly utilized implant in clinical practice in orthopedics, dentistry, and other hard tissue implant materials [3]. Innovative Ti-alloys, including Ti-Zr alloys, have recently gained much interest in biomedicine. Improved corrosion resistance has been seen in the Ti-Zr binary alloys. The micro-hardness was increased, Young's modulus decreased, and the biocompatibility was enhanced or maintained compared to CP-Ti/Ti-6Al-4V [4]. However, titanium-based implants have some drawbacks, including bacterial infection susceptibility, inadequate bone-bonding capacity in clinical applications (low osteoconductivity), and the danger of implant loosening because of wear debris formation at the implant-bone interface [5]. Also, the possibility of forming fibrous tissue at the interface between implant and bone impedes the bonding between host tissue and implant. The success of titanium-based implants is directly impacted by how well their surfaces function at interacting with surrounding tissue [6,7].

Studies have proven to modify and functionalize the surface of Ti-based substrate to give unique biological features to the implants [8]. However, many techniques reported in the literature concentrate exclusively on increasing cell adhesion or

845

avoiding bacterial infections, and their combined benefits are seldom investigated. A single functionalized surface is no longer adequate because antibacterial and osteogenic functionalization is often at odds [9]. Implants with antimicrobial functionalization, for instance, are frequently made with a degree of cytotoxicity and tissue toxicity, which reduces the implant's ability to connect with the surrounding tissue [10]. Similarly, implant surfaces with osteogenic functionalization may promote bacterial cell-like actions and encourage biofilms' formation [11]. As a result, there is a growing interest in developing implants that are highly resistant to bacterial infection while stimulating bone bonding [12].

Among the surface, factionalized methods coating with polymeric matrices filled with bioactive ceramic nano-particles are more attractive. They can apply more than one material simultaneously, making a composite and utilizing the beneficial characteristics of each component. Dip coating, spin coat, electrospinning, plasma spray, electro force, and other coating technique was utilized to increase bioactivity and osseointegration while preventing bacterial infection on the surface of Ti-based implants [13].

Chitosan (CS) is a naturally occurring polysaccharide that has shown promising results as a tissue engineering agent. As deacetylated from chitin, chitosan is a linear polysaccharide composed of glucosamine and N-acetyl glucosamine units connected to glycosidic linkages. According to reports, it has a high affinity for proteins and is nontoxic, hydrophilic, antibacterial, and biodegradable [14,15]. Polycaprolactone (PCL) is a biocompatible and biodegradable aliphatic polyester. It has several desirable characteristics, including being harmless to the organism, resorbing slowly after implantation, and having desirable mechanical qualities [16].

To balance chitosan's very hydrophilic nature and poor mechanical qualities, PCL/CS composites such as membranes and porous scaffolds have been developed [17]. Lack of bioactivity is now the critical factor limiting PCL/CS composite use in tissue engineering. In order to improve bone bonding and osteoblast proliferation, a unique ceramic substance was added to the PCL/CS blend [18,19].

Hydroxyapatite (HA) $Ca_{10}(PO_4)_6(OH)_2$ is biocompatible, osteoconductive, and displays outstanding chemical and biological affinity to bone tissue. It has structural and chemical similarities with the mineral component of human hard tissue. It is widely known that bone mineral has a Ca/P ratio of around 1.5 and a calcium-deficient apatitic (cd-HA) structure. In addition, they discovered that the polymer–HA contact significantly impacts mechanical properties [20].

As a result of its biocompatibility, chemical stability, and antimicrobial properties, the application of titanium dioxide TiO_2 with polymer to form a coating on titanium-based implants has been proposed as a potential method to improve tissue-implant interactions while simultaneously preventing bacterial colonization [21].

Strontium (Sr), an essential trace element, may promote bone production by encouraging osteoblast development and decrease bone resorption by blocking osteoclast differentiation. Approximately 98% of the strontium in our bodies is found in bone tissue, where its anabolic and antiresorptive properties positively influence bone metabolism. Because of their structural and mechanical qualities, incorporating strontium components such as $SrTiO_3$ into polymer coatings can potentially increase osseointegration and the differentiation of pre-osteoblast cells [22,23].

This research aims to overcome the inert surface of metallic implants, weak osteoconductivity, and risk of bacterial infection by creating an active composite coating layer that enhances pre-osteoblastic cell adhesion, proliferation, and differentiation and, at the same time, resists bacteria. Three nano-ceramic (nHA, $nTiO_2$,$nSrTiO_3$) materials were used as filler material and individually added to the blended of PCL/Chitosan to form three types of composite (PCL/Chitosan/nHA, PCL/Chitosan/$nTiO_2$, PCL/Chitosan/$nSrTiO_3$), and then used in electrospinning coating technique to develop coating layer of nanocomposites fiber on the surface of Ti-25Zr alloy. The nano-fiber coating layer's high surface area of contact and porosity improves the functionalized surface [24]. Nanoscale structures on Ti-based implants increase bone bonding and reduce fibrosis by stimulating preosteoclast adhesion and proliferation.

2. Materials and methods

2.1 Materials

Titanium powder (sigma Aldrich150-200 μm 99.7 purity USA), Zirconium powder (sigma Aldrich100-150 μm 99.5 purity, USA), Chitosan nanopowder (medium molecular weight, 90% deacetylated, APS 80nm) was obtained from (Hongwu International Group, China). Polycaprolactone (Mη = 80 000 sigma Aldrich USA), Nano ceramic (HA, TiO_2, $SrTiO_3$,) all in range (80-100 nm) supply from (Jinan Boss Chemical Industry China), Acids (acetic, formic, sulfuric, hydrochloric) acetone was purchased from (Thomas Baker Chemicals India) and where all of the analytical grade.

2.2 Base Material Preparation

Ti–25Zr disc (15mm diameter, and 2mm height) base metal was prepared using the powder metallurgy technique. Titanium powder was mixed with 25 wt. % Zirconium powder for 6 hours, then the mixed powder was compressed at 500 MPa. The green compact disc was then sintered in vacuumed furnace10^{-3}torr at a range of 10°C/min, held for 2 hours at 1300°C temperature, and left to cool in the furnace.

2.3 Surface Treatment of The Base Sample

The Ti-25Zr samples were mechanically polished with 120-1000 grit silicon carbide paper. The samples were cleaned for 20 minutes using an ultrasonic clean path with acetone followed by deionized water. The surface of the metal implant was made rougher by treating it with a combination of H_2SO_4: HCl: H_2O (1:1:1) at 60°C for one hour. In addition, samples were alkaline-treated with 10 M NaOH at 60°C for 24 hours and left to dry overnight.

2.4 Porosity Test

The porosity of the sintered Ti–25Zr alloys is determined by an Equation:

$$p = 1 - \frac{\rho}{\rho_\circ} \times 100\% \tag{1}$$

where ρ is the apparent density of the alloy, which is determined by the liquid displacement method using Archimedes' principle. ρ_0 is the nominal theoretical density of the corresponding alloy, calculated as

$$\rho_\circ = \frac{1}{\left(\frac{A\%}{\rho_A}\right) + \left(\frac{B\%}{\rho_B}\right)} \tag{2}$$

where A% and B% are the mass percentage of elements A and B, and ρ_A and ρ_B are the theoretical density of A and B.

2.5 Mechanical Evaluation of Base Sample

A Vickers digital microhardness (HVS-1000, Laryee technology, China) tester with a load of 9.8N and a dwell period of 15s was used to measure the hardness of the samples according to (ASTM E384). The local values from 10 points were used to find the average microhardness values. The compressive stress measurement was done at room temperature using the Brazilian method (ASTM. D3967-95a) for the sample (15 mm diameter, 18 mm height) (a universal tensile machine made in China by Instron). Lastly, the elastic modulus was found by using (Ultrasonic type CCT-4 UK Tester) and solving the following Equations:

$$\upsilon = 1 - \frac{1}{2} \cdot \frac{1}{1 - (C_{trans}/C_{long})^2} \tag{3}$$

$$E = 2 \cdot \rho \cdot (1 + \upsilon)\, C_{trans}^2 \tag{4}$$

where: $_{trans:}$ is the transverse wave speed, C_{long} :is the longitudinal wave speed, υ: is the Poisson modulus, E: is modules of elasticity, ρ: density of the material (the density value assumes an isotropic, homogeneous, and nondispersive material. The error was estimated with an error propagation with a 95% confidence level).

2.6 Preparation of Electrospinning Solutions

Chitosan 2% (w/v) was dissolved in 4/6 acetic/formic (v/v) acid (100 ml) using a hot plate magnetic stirrer for 12 hours at 50 $^\circ$C to make a Chitosan solution. PCL 8% (w/v) was added to the Chitosan solution and stirred for 3 hours until a clear and homogenous solution of the PCL/Chitosan blended forms. The nHA, $nTiO_3$, and $nSrTiO_3$ were added individually, each with 1% (w/v), and stirred for 1 hour to form three solutions. Then each solution was then homogenized for 3min using a homogenizer (Model 300VT Ultrasonic Homogenizer USA). To make the PCL/Chitosan/nHA (HA1), PCL/Chitosan/$nTiO_2$ (TI1), and PCL/Chitosan/$nSrTiO_3$ (SR1) solutions ready for electrospinning coating.

2.7 Electrospinning

The prepared solutions were placed in a 5-ml syringe fitted with a blunt-end 22 G needle. Using an infusion pump. The fluid was expelled at a rate of 1 ml/h (Kd scientific syringe pump 200, USA). The needle tips' distance from the grounded sample was maintained at 10 cm. The needle was subjected to a high voltage of 20 kV. The relative humidity in the room ranged between 30 - 50%. Before the examination, the fibers were dried overnight and kept in a desiccator.

2.8 Characterization of The Non-Coated Base Sample

The crystal phase was characterized by X-ray diffraction performed with Cu Ka radiation operated at 40 kV and 40mA at room temperature (XRD, 6000 Shimadzu, Japan). The Microstructures and surface topography of the samples were examined by scanning electron microscopy (SEM, TESCAN VEGA3, Czech Republic). The chemical composition and homogeneity of sintered samples were investigated using energy-dispersive spectrometry (EDX), efficiently combining SEM imaging with elemental composition analysis.

2.9 Characterization of Coatings

The microstructures of the electrospun fibers were sputtered with gold before being examined using a field emission scanning electron microscope (FESEM) (Inspect F-50, Spain) at an accelerating voltage of 15 kV utilizing secondary electron (SE). The existence of (nHA, $nTiO_2$, $nSrTiO_3$) in the PCL/Chitosan polymer blend was confirmed using a dispersive energy X-ray (EDX) linked to a FESEM.

2.10 ATR-FTIR

Attenuated total reflection-Fourier Transform Infrared Spectroscopy ATR-FTIR (Bruker Tensor 27 IR, Germany) investigated the functional chemical groups. The FTIR spectra were recorded between (4000-500) cm^{-1} region using a universal ATR sampling accessory.

2.11 Wettability Evaluation

The wettability of a surface was assessed using the sessile drop technique with DD water. A volume of 1 µml of distilled water was dropped onto the coated surface, and the contact angle of the water was measured for a duration of 10 seconds. This test was repeated three times to ensure accuracy, and the contact angle was measured using a camera-based contact angle meter.

2.12 Antibacterial Test

The Inhibition Zone technique was utilized to assess the antibacterial activity of electrospun coating fibers and a bare Ti-25Zr sample against Staphylococcus aureus and Streptococcus mutans bacteria. Nutrient agar plates were inoculated with 1 mL of a bacterial solution (10^8 CFU/mL) using the spread plate method. A 1.5 cm diameter circular layer of the nano-fiber coating substrate was placed on the plates, which were then incubated at 37°C for 24 hours. Inhibition zones were determined by measuring the clear regions surrounding each electrospun nano-fiber sample.

2.13 In Vitro Cell-Material Interactions

2.13.1 Samples sterilization

Before cell seeding, samples were UV-sterilized for 20 minutes, submerged in 75% ethanol for 1 hour, and rinsed with PBS at least three times, each for 15 minutes.

2.13.2 Cell culture

The MC3T3-E1 cell line was obtained from the Pasteur Institute (Tehran, Iran). Cells were cultured in a humidified incubator with 5% CO_2 in air at 37°C and maintained in Dulbecco's Modified Eagle Medium (DMEM; Gibco, Life Technologies, Waltham, MA, USA) supplemented with 10% fetal bovine serum (FBS; BioWest SAS, Nuaille, France) and 1% PSF (antibiotic antimycotic solution, Sigma-Aldrich®, St. Louis, MO, USA). When cells were 75% confluent, they were detached at 37°C in phosphate-buffered saline (PBS) containing 0.25% trypsin (Gibco, Invitrogen, Waltham, MA, USA) and 0.1% ethylenediaminetetraacetic acid (Merck, Darmstadt, Germany). After that, we resuspended the cells in DMEM supplemented with 10% FBS and 1% PSF.

2.13.3 Cell seeding

At a density of 10,000 cells per well on 24-well culture plates, five 40 µl drops of the cell suspension were carefully distributed throughout the surface of the samples. Following a 30-minute attachment period, the medium was introduced to the cell/sample complexes.

2.13.4 Cell Viability Assay

MC3T3-E1 cell viability on the samples was estimated using AlamarBlue assay (Sigma-Aldrich, St. Louis, MO, USA); briefly, 1 ml of 10%(v/v) AlamarBlue solution was added to each well and incubated for about 4 hours, then the absorbance was determined at 530/560 nm using an ELISA Reader (Stat Fax-2100, Miami, FL, USA). The cell viability was quantified by dividing the sample's absorbance by the absorbance of the control on day 1, 3, 7. Data were obtained from three independent experiments (n=3).

2.13.5 Cell Proliferation

MC3T3-E1 pre-osteoblast proliferation was evaluated by determining the cell number in the samples at days 1, 3, and 7 and using AlamarBlue® fluorescent assay. At each time point, samples were transferred to a new plate, AlamarBlue® was added, and the fluorescence was measured. After performing the AlamarBlue® assay each day, samples were washed twice with PBS and incubated in the osteogenic medium in a humidified incubator with 5% CO_2 at $37^°$C. Data were obtained from three independent experiments (n=3).

2.13.6 Cell morphology

To investigate cell morphology on samples using scanning electron microscopy (SEM), cell-seeded samples were fixed with 4% glutaraldehyde on day 7, followed by dehydration in a graded ethanol series (50, 70, 80, 90, 100%; each step 3 min), and then dried at room temperature. The fixed cell-seeded were coated with gold using (Edwards Sputter Coater S150B, Burgess Hill, UK) and viewed using a scanning electron microscope (Zeiss EVO LS-15, Oberkochen, Germany) at a 20 kV accelerating voltage.

3. Results and Discussion

3.1 Microstructures and Chemical Composition of Ti-Zr Alloy

X-ray diffraction analysis (XRD) was used to determine the phase compositions of the alloys developed. Figure 1 shows the typical XRD profiles of Ti–25Zr alloys after 2 hours of sintering at 1300°C. The XRD data indicate that the main phase of the Ti–25Zr alloy was the α hcp phase. The complete solid solution system of Ti and Zr may explain why Ti–25Zr alloys display the α phase. In addition, the higher atomic radius of Zr (1.62 A°) compared to Ti (1.47 A°) causes the addition of Zr to

raise the phase lattice parameters, resulting in a shift of the XRD peaks toward a low angle. This finding corresponds well with those reported by [25,26].

The chemical composition and uniformity of sintered samples were evaluated using energy-dispersive X-ray spectroscopy (EDX). The findings of the semi-quantitative chemical analysis conducted by the (EDX) in point are shown in Figure 2. The EDX examination revealed the homogeneity and purity, indicating that no additional element is present in the powder combination, and Table 1 shows the proportion of elements, revealing the appropriate mixing procedure.
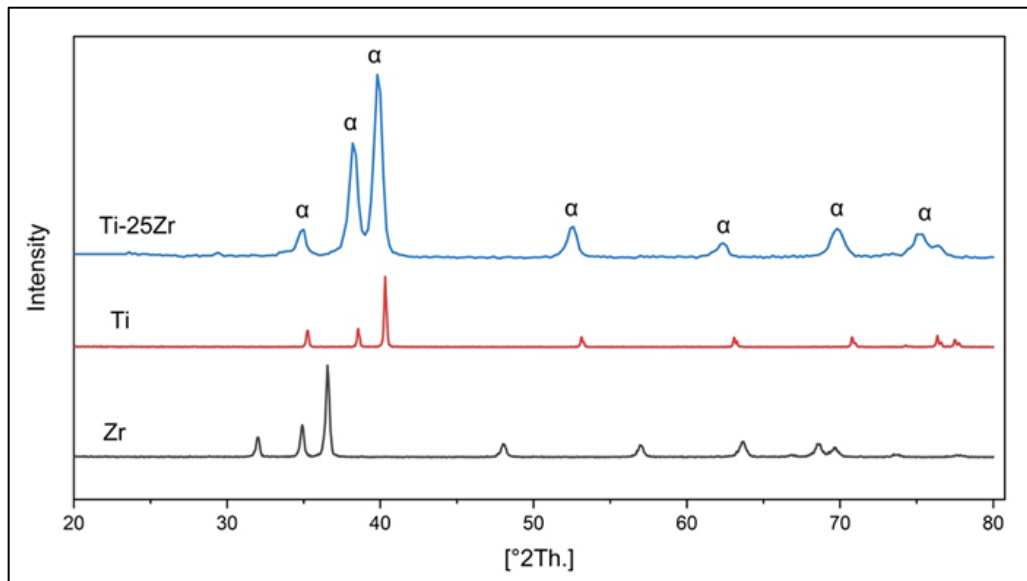
Figure 1: XRD patterns of pure Ti, pure Zr, and Ti–25Zr alloys
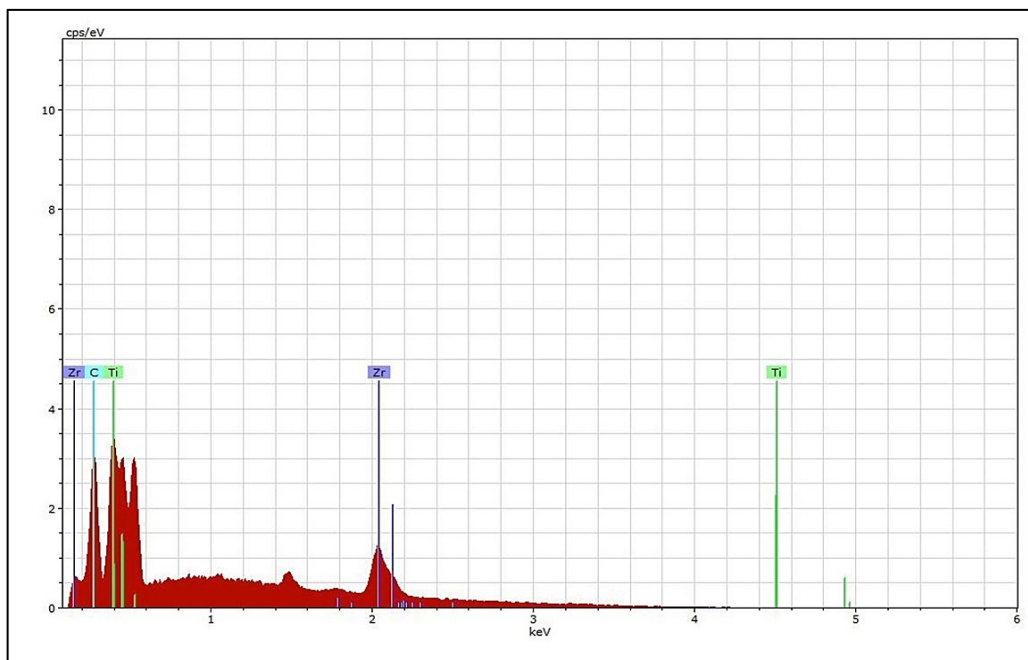
Figure 2: EDX spectrum for substrate Ti-25Zr alloy

Table 1: The EDX analysis in point for Ti-25Zr alloy

Element	Weight %	Atomic %	Error %
ZrL	23.95	15.23	9.8
TiK	74.65	79.24	6.37
CK	1.4	5.53	0.38

3.2 Surface Morphology

There were clear morphological differences between the treated and untreated surfaces of the Ti-25Zr samples. Ground grooves in the surface of the control sample served as a benchmark for comparison Figure 3a. The grooves were easily visible

after being etched with acid and alkali Figure 3b. At the same time, the nanosized pit Figure 3c, after treatment, seemed to deepen and sharpen Figure 3d.
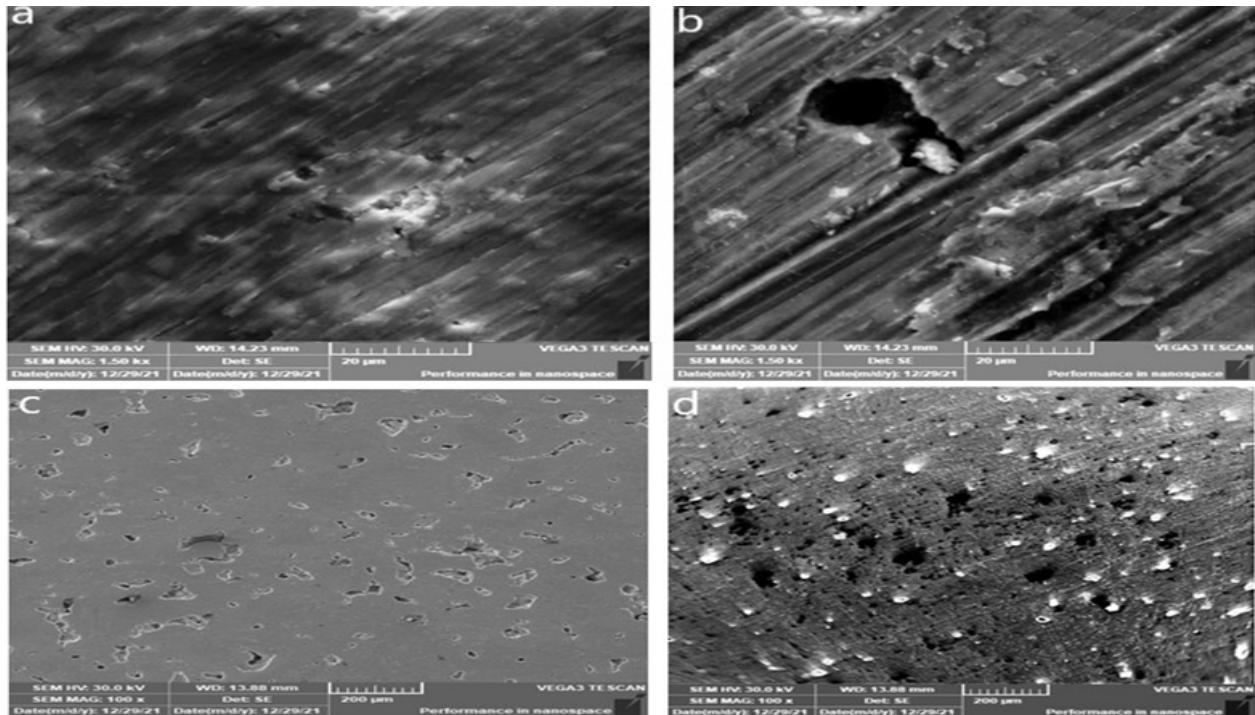

Figure 3: Scanning electron microscopy (SEM) images of the textured surface before (a,c) and after (b,d) acid and alkaline treatment

3.3 Mechanical and Physical Characterizations

Microhardness, tensile, compressive, Modulus of Elasticity, porosity, and density of Ti-25Zr are listed in Table 2.

Table 2: Mechanical properties of Ti-25Zr alloy prepared by powder metallurgy

Microhardness, Hv	Compression stress, MPa	Modulus of Elasticity, GPa	Porosity %	Apparent density
283±21	713±79.3	78±8.1	9±0.36	4.46 ±0.02

The impact of zirconium contents on the mechanical characteristics of Ti-25Zr alloys was to enhance all mechanical properties over cp-Ti, as previously indicated [27,28]. The toughness of Ti-25Zr alloys rose inversely with Zr content [25]. Because the substitution of Zr resulted in crystalline lattice deformation and atomic displacement restrictions. Furthermore, the Ti-25Zr alloys were complete solid solutions with hardness increases, which were most likely generated by solid solution hardening of the α phase and the contribution of the refined microstructure [29].

A modest quantity of Zr significantly improves the alloy's compressive and tensile strength. [25]. Two factors most likely caused the increase in compressive and tensile strength caused by alloying. First, according to the Ti-25Zr alloy phase diagram, the α phase indicated a total solid solution with no intermetallic compound. As a result, the solid solution mechanism would create more obstacles for the slip system, increasing mechanical properties. Then, according to the Hall-Petch formula, fine grain strengthening increases alloy yield strength. The phase transition starting temperature fell as Zr increased, inhibiting α phase expansion. Grain refining increased grain boundary area, leading to more excellent resistance to dislocation glide and improved mechanical properties [30].

3.4 Composite Fibers Characterization.

Field-emission scanning electron microscopy (FESEM) was used to visualize the morphology and density of the nanocomposite fiber. Average fiber diameter and porosity were analyzed using (ImageJ, National Institutes of Health, Bethesda, MD). Chemical elements were detected using energy dispersive X-ray spectrometer (EDX). For all three types of nano-fiber composite coating (HA1, TI1, SR1), bead-free homogeneously distributed non-woven fibers can be observed in Figure 4-6 a.

EDX analysis Figure 4 b shows that the coating layer consists of calcium and phosphate elements. The fiber diameter for (HA1) ranged from (41.76 to 602.31nm) with a mean diameter of (286.45 ± 17.87nm) and an average porosity of (1523.86± 121.55nm) Figure 4c-d. EDX analysis for TI1 Figure5 b shows that fiber-containing titanium belongs to TiO_2. While the fiber diameter of (TI1) ranges from (82.22 to 224.42nm) with a mean diameter of (123.45 ± 4.94nm) and a mean pore size of (923.81± 73nm) Figure5 c-d,

The EDX analysis for SR1 Figure 6 b proves the presence of strontium related to the addition of SrTiO$_3$ to the precursor. Figure6 c-d Shows that (SR1) fiber diameter range (111.23 to 321.197nm) with a mean diameter of (195.54 ± 9.25nm) and a mean pore size (1615.99± 96.11nm).
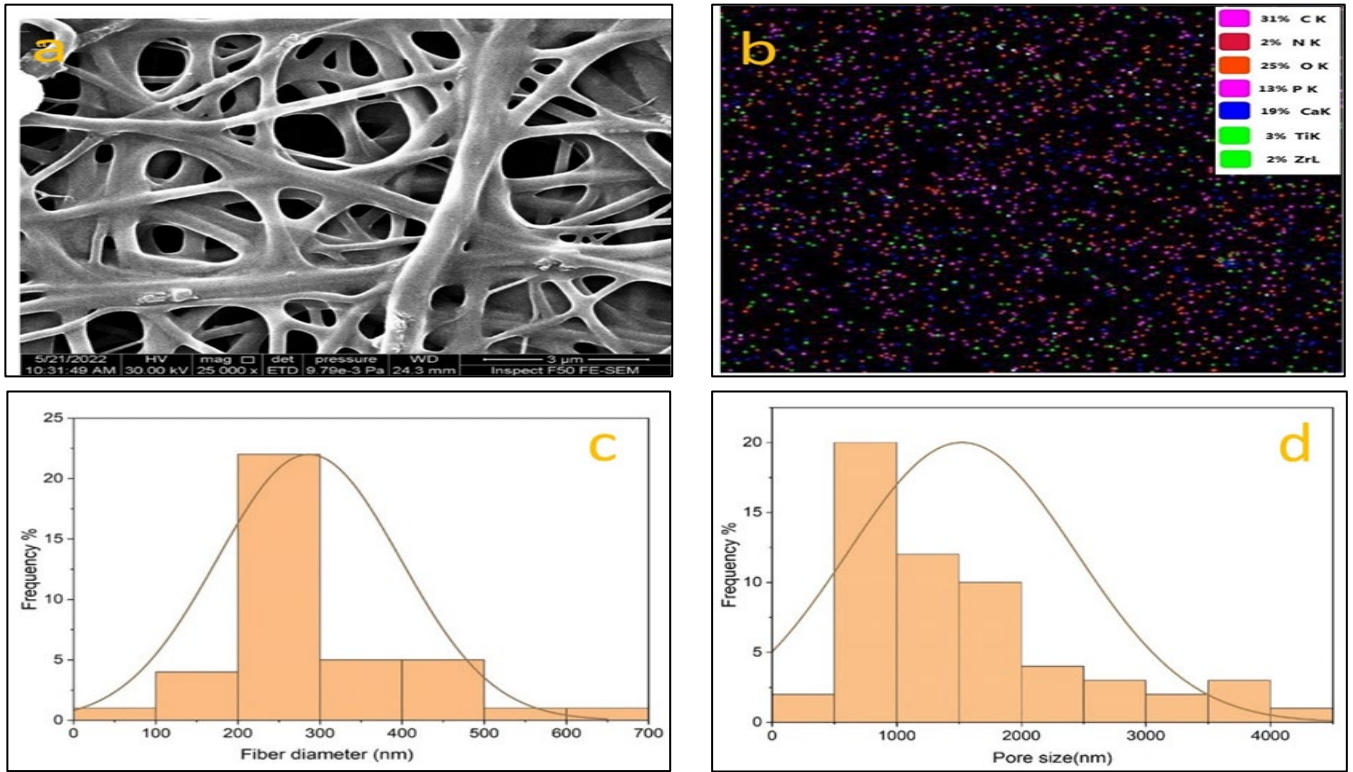

Figure 4: FESEM (a), EDX (b), fiber diameter histogram (c), pore size histogram (d),for PCL/Chitosan/nHA (HA1) nanocomposite fiber
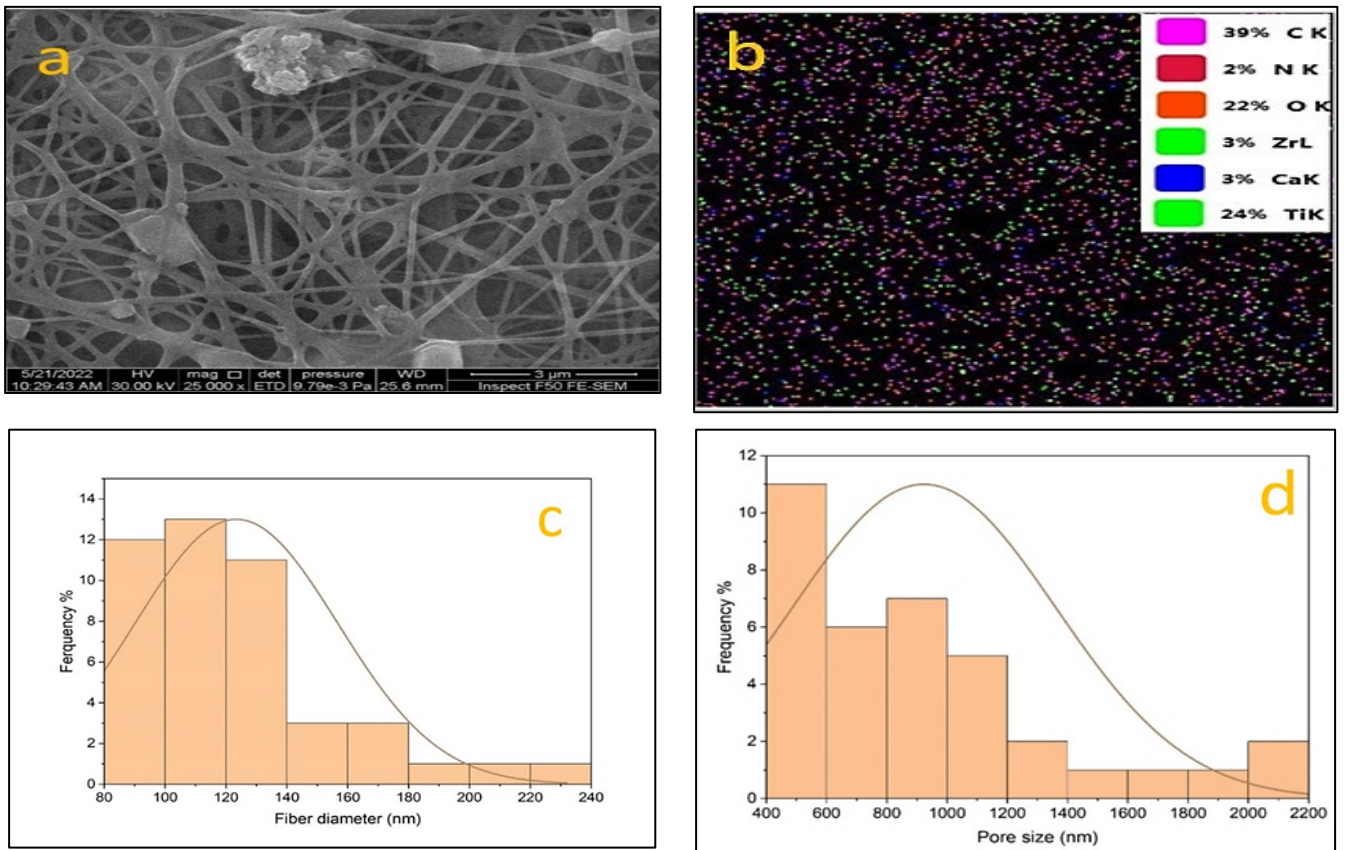

Figure 5: FESEM (a), EDX (b), fiber diameter histogram (c), pore size histogram (d).for PCL/Chitosan/nTiO$_2$ (TI1) nanocomposite fiber
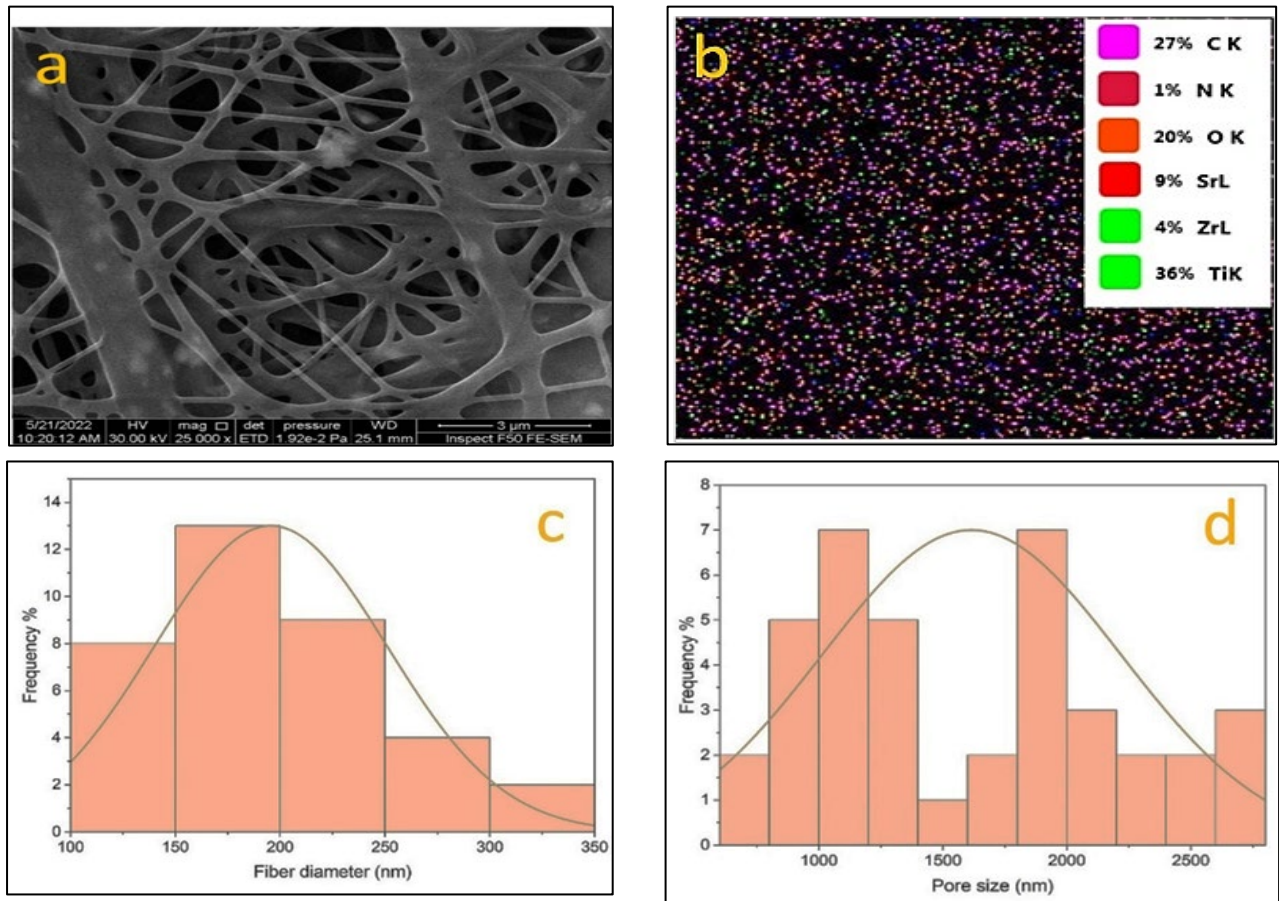
Figure 6: FESEM (a), EDX (b), fiber diameter histogram (c), pore size histogram (d)for PCL/Chitosan/nSrTiO$_3$ (SR1) nanocomposite fiber

3.5 Fourier Transform Infrared Spectroscopy (FTIR)

The FTIR spectra of polycaprolactone, chitosan, ceramic nano-additive, and the composite coating of (PCL/Chitosan/nHA, PCL/Chitosan/nTiO$_2$, PCL/Chitosan/nSrTiO$_3$),electrospun fiber are shown in Figures 7-9, respectively. The primary peak in the pristine PCL spectra is at 1723 cm^{-1}, which relates to the carbonyl group of the ester group. In addition, displayed an asymmetric CH$_2$ stretching peak at 2943cm^{-1} and a symmetric CH$_2$ stretching peak at 2869 cm^{-1}. The absorption peak at 1294 cm^{-1} related it to the C–O and C–C stretching modes, and bands at 1239, 1161,1107,1045 cm^{-1} attributed to asymmetric and symmetric C–O–C stretching [31].

The intense chitosan peak was identified at 1726 cm^{-1} of carboxylate ion, and the chitosan spectra revealed a broad band of about 3245 cm^{-1} linked with O-H and N-H stretching vibrations.; peaks at 2945 and 2897 cm^{-1}, corresponding to asymmetrical and symmetrical methylene groups, and an 1180–1063 cm^{-1} range, characteristic of its saccharide structure, were also detected. Interestingly, the chitosan band associated with the C=O stretching of amide I centered generally at 1615 cm^{-1}. At the same time, the peak at 1510 cm^{-1} is attributed to the amideII band. In addition, the characteristic band due to C-C aromatic stretch occurring at 1420 cm^{-1} was also present in the sample. Three peaks are situated between 1020 to 1140 cm^{-1} related to C-O-C stretching asymmetric and symmetric mode [32,33].

From Figure 7, the presence of hydroxyapatite is initially indicated by the presence of a wide FTIR band centered at around 1017-1087 cm^{-1}. The bands at 875–962 cm^{-1} and 557–600 cm^{-1} relate to the n1 and n4 symmetric P-O stretching vibration of the PO$_4^{-3}$ ion. As a significant peak of a phosphate group, the n3 vibration peak could locate a range between 1017 cm^{-1} and 1087 cm^{-1}, where the most significant degree of asymmetry presented a peak among the PO$_4$ group. The band between 557 cm^{-1} and 600 cm^{-1} belongs to n4, doubly degenerate asymmetric O- P-O bending mode of the PO$_4^{-3}$ tetrahedron. The weak mode at 625 cm^{-1} can be attributed to the OH liberational mode of the OH group in the HA lattice. Moreover, the peaks at 1420 cm^{-1} correspond to OH bonds in HA [34,35].

The PCL/chitosan/nHA nanocomposite spectra are distinct from those of pure nHA. Approximately 25 cm^{-1} of the phosphate group's absorption peak was displaced. PCL/Chitosan/nHA nanocomposite spectra revealed more dramatic shifts in the location and intensity of peaks related to chitosan's amino and amide groups. This suggests that the nHA interacts well with the polymer matrix, particularly the chitosan component [31].

Figure 8, shows the FTIR spectrum of TiO$_2$ nanoparticles. From the FTIR spectrum of TiO$_2$ nanoparticles, the Ti-O bending mode is shown at 558-672 cm^{-1}, while the peak at 551 cm^{-1}is ascribed to Ti–O–Ti bonds in the TiO$_2$ lattice. Asymmetrical and symmetrical stretching vibrations of a hydroxyl group OH may be observed at 3188 cm^{-1}. The band at

1630 cm^{-1} may be attributed to water adsorbed on the TiO$_2$ surface. The peak around 1043 cm^{-1} may be due to C-O stretching. These results reasonably agree with earlier reports [36].

The FTIR spectrum of PCL/Chitosan/nTiO$_3$, which contains 1 wt% nTiO$_2$, exhibited similar behavior. A possible interaction between the TiO$_2$ and Chitosan network is suggested by the fact that the bands identified are similar to one another, with only minor adjustments to band location and relative intensity [37].

Due to matrix change and interfacial contact between organic and inorganic phases, this may reduce the chitosan matrix's crystallinity (drop in intensity of -OH and -NH bands). However, all TiO$_2$ impacts on the chitosan structure depend on variables, including the size and concentration of TiO$_2$ nano-particles and the number of free amino groups present, which causes TiO$_2$ to interact with chitosan [38].

Figure 9, the incorporation of SrTiO$_3$ NPs may be analyzed for absorption using FTIR spectroscopy. The bending and stretching vibrations of the TiO$_6$ octahedron are still visible in the spectra, as are the major wide absorption bands with their centers at 425 and 650 cm^{-1}. The surface hydroxyl group's OH$^-$ stretching vibration is first assigned to and characterized by the absorption at 3300 cm^{-1}. H-O-H bending vibration of physically adsorbed water has been attributed to the remaining minor peak at about 1630 cm^{-1} [12]. Slight shifts in the wavenumber of the nSrTiO$_3$ constituents are evidence of the successful development of physical interaction between the constituents and the total synthesis of the new nanocomposite (PCL/chitosan/ nSrTiO$_3$).
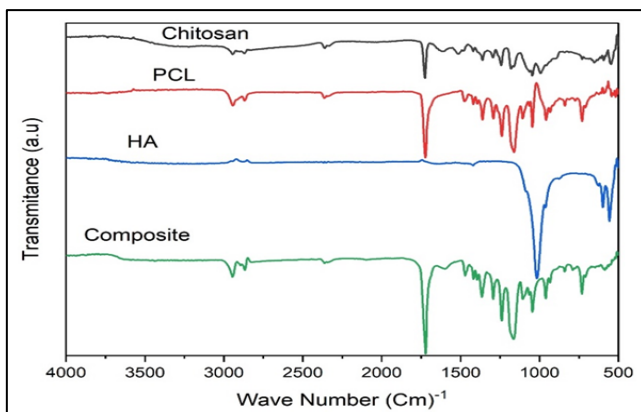

Figure 7: FTIR spectra of pure (PCL, Chitosan, Nano-HA) and composite (8% w/v PCL,2% w/v Chitosan, 1% w/v Nano-HA)
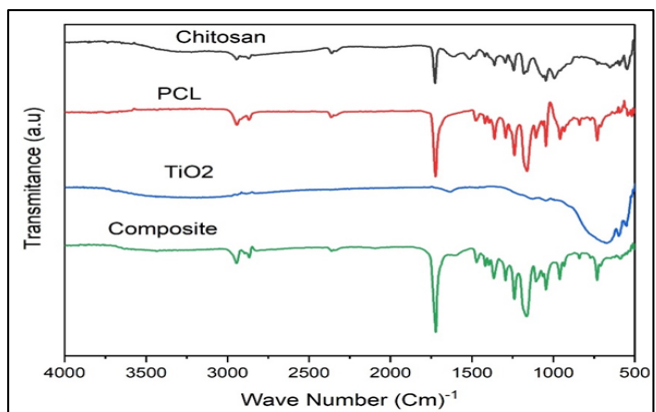
Figure 8: FTIR spectra of pure (PCL, Chitosan, Nano-TiO$_2$) and composite (8% w/v PCL,2% w/v Chitosan, 1% w/v Nano-TiO$_2$)
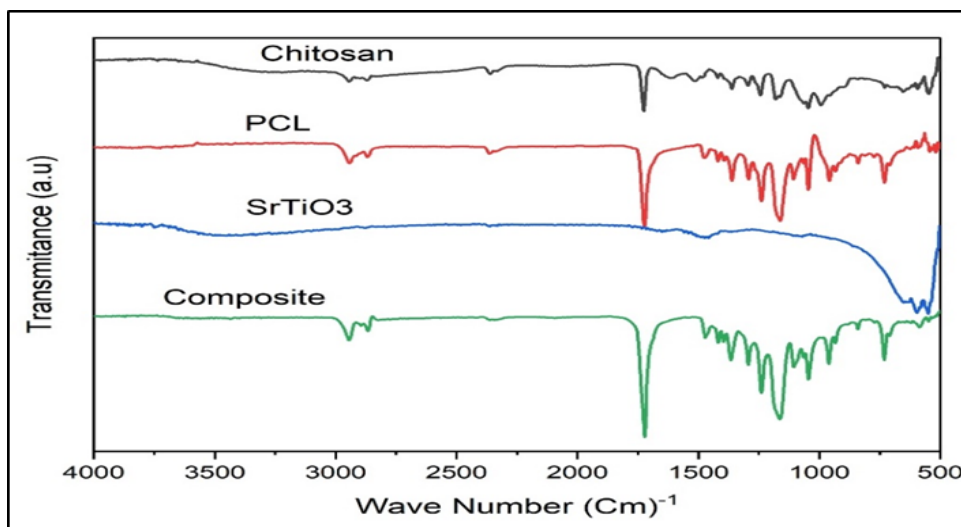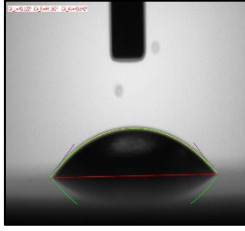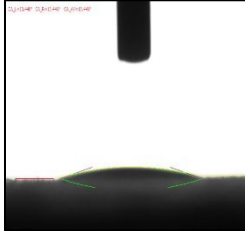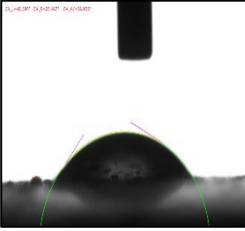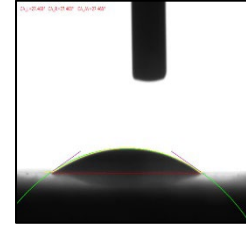

Figure 9: FTIR spectra of pure (PCL, Chitosan, Nano-SrTiO$_3$) and composite (8% w/v PCL, 2% w/v Chitosan, 1% w/v Nano- SrTiO$_3$)

3.6 Contact Angle

The surface of a metallic implant is the primary interface between the implant and the body. Adsorption of serum proteins and the adhesion behavior of osteoblasts and bacteria may be significantly affected by the hydrophilicity of the metal surface. The contact angle measurements of the three Coating samples and the control sample, as given in Table 3, revealed angles ranging from 43.0° to 13.0°, indicating that the surfaces of all samples were hydrophilic.

Table 3: Contact angle measurements of the different types of the composite coating and control sample

Sample	Control(Ti-25Zr)	HA1(PCL/CS/nHA)	TI1(PCL/CS/nTiO2)	SR1(PCL/CS/nSrTiO3)
Contact angle	43.642°	13.446°	36.932°	27.468°

Control sample Ti-25Zr has low wettability. However, after acid and alkaline treatment that increases surface energy and roughness, the contact angle values became significantly lower and changed from hydrophobic to Hydrophilic with a contact angle of 43.642°, which is beneficial for cell adhesion and increased biocompatibility [27,39].

The results further show that the composite coating sample wettability improved. All the coatings were hydrophilic due to their surfaces' high porosity and roughness, the amino groups present there, and the chitosan's hydroxyl group, which is linked with the hydrogen in water molecules, reduced their hydrophobicity [40].

As can see in Table 3, the composite coating containing Nano-hydroxyapatite (PCL/chitosan /nHA) shows a low angle of 13.446°, which may contribute to the presence of (nHA), improves the hydrophilicity and, together with chitosan, improve the wettability. This result agrees with [41]. Nano strontium-titanate is also reported to increase hydrophilicity in biomedical applications, so (PCL/chitosan/nSrTiO$_3$) also showed good wettability with a contact angle of 27.468°[42]. Nano Anatase TiO$_2$ with hydrophilic properties also enhanced the wettability of coated surface and expressed a 36.932° contact angle [43,44].

3.7 Antibacterial Evaluation.

Due to its high biodegradability, nontoxicity, and antibacterial characteristics, chitosan is often used as an antimicrobial agent, alone or in combination with other natural polymers [38]. The addition of the filler nano-ceramic (nHA, nTiO$_2$, nSrTiO$_3$) used with chitosan was also reported as antibacterial material, improving the overall inhibition zone around the coating implant. Staphylococcus aureus (S. aureus) and Streptococcus mutans (S. mutans) bacteria were used in the antibacterial test. All the composite coating (PCL/Chitosan/nHA, PCL/Chitosan/nTiO$_2$, PCL/Chitosan/nSrTiO$_3$) show good antibacterial effects with comparable results in both kinds of bacteria, and the results are shown in Table 4 and Figure 10.
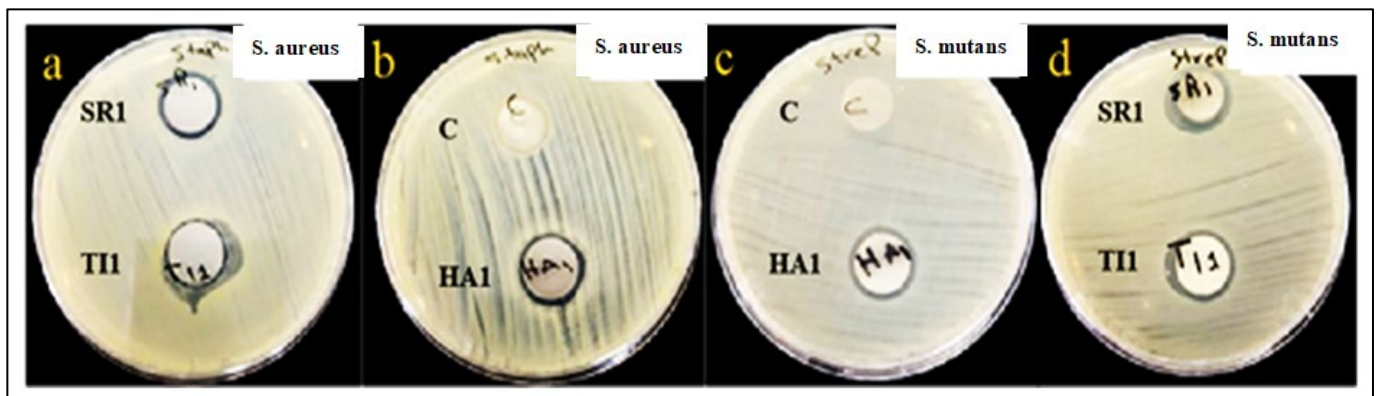
Figure 10: Shows the antibacterial inhibition zone of the three types of composite coating (HA1, TI1, SR1) and control samples (C) Ti-25Zr without coating in (a-b) Staphylococcus aureus (S.aureus) and (c-d) Streptococcus mutans (S.mutans)

Table 4: Antibacterial analysis of the coating with gram-positive S. aureus and S. mutans

	Inhibition zone (*S.aureus*)(mm)	Inhibition zone (*S. mutans*) (mm)
Control	0	0
HA1	17	18
TI1	17	19
SR1	18	20

The result shows no bacterial resistance in the control sample with no coating layer, which increases the risk of infection due to their susceptibility to bacterial colonization. The maximum inhibition zone was found with a coating containing SrTiO$_3$, attributed to Sr$^+$ ion release, a relevant antimicrobial effect, and a biofilm inhibition potential against, as they reported

previously [45]. Coating with the addition of TiO_2 has inhibition results comparable to $SrTiO_3$, so it also had antimicrobial resistance, as mentioned in many research studies [46]. Hydroxyapatite incorporated with coating also shows good resistance to both kinds of bacteria [47].

3.8 Cytocompatibility

3.8.1 Cell Growth and morphology

Cell reaction to biomaterial surfaces is regarded as one of the essential criteria in defining material biocompatibility. Cell activity was assessed on days 1, 3, and 7 to determine the cytocompatibility of the Ti-25Zr coated samples and compared to a control sample (bare Ti-25Zr). Figure 11a shows the cell viability percentage for the MC3T3-E1 cells using the AlamarBlue test on samples. On day 7, all samples had a high cell viability percentage. However, they have a low percentage in 24 hours, which may be attributable to the trace of organic solvent used in the surface treatment of the control sample and also used in the creation of the coating layer in coated samples, but they dramatically grow in 3 and 7 days of culture.

Higher cell proliferation is often the outcome of better cell adherence. In this work, the AlamarBlue test was used to examine cell proliferation on different samples after cluttering for 1, 3, and 7 days; the fluorescence intensity of diminished AlamarBlue displayed the cell proliferation levels.

As shown in Figure 11b, cell proliferation demonstrated a significant increase in cell number on all of the sample surfaces as a function of time; however, the cell number was higher on the (HA1) coated sample because the electrospun fiber layer contains nano-hydroxyapatite, which serves as a source of calcium and phosphate ion release. As a result, the surface remineralized, and the bioactive apatite layer formed when nano-particles were hydrated in the culture environment [48].
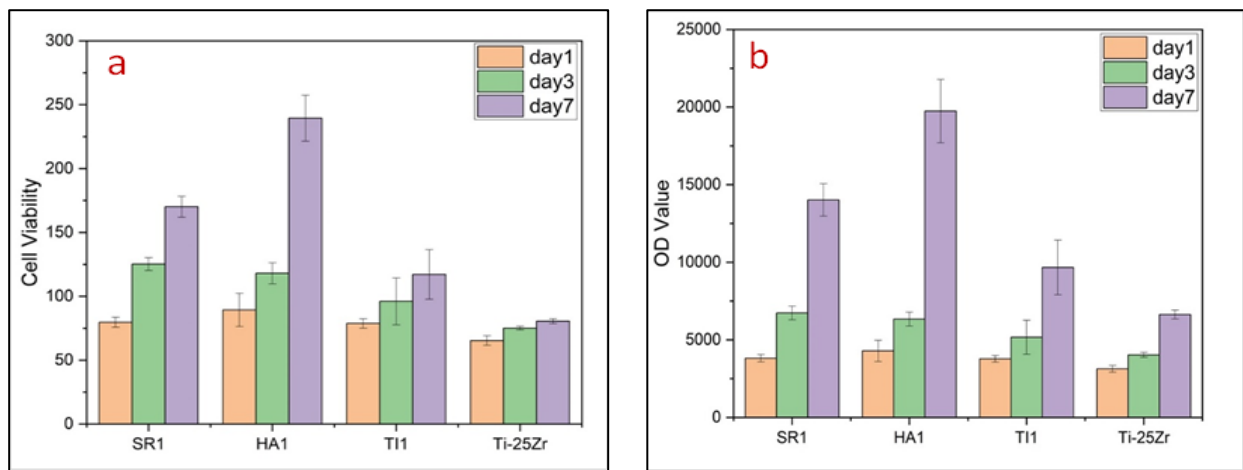

Figure 11: (a) Cell viability and (b) proliferation assay on coated and non-coated samples

Nano-fiber coating layer with strontium titanate nano-particles (SR1) also demonstrates high cell proliferation, which is supported by previous studies. Sr^{2+} ions promoted cell proliferation and indicated cell viability increase, which may be attributed to the activation of calcium-sensing receptor CaSR and the ability of Sr to enhance differentiation of pre-osteoblastic cells and osteoclast inhabitation [11,49].

Antise TiO_2 nano-particles with hydrophilicity, hemocompatibility, and protein adsorption are present in (TI1) nano-fiber coating surfaces, which also have excellent cell number and cellular behavior. However, (TI1) continues to be less than (HA1) and (SR1) in comparison[50]. The viable cell number was higher in all coating samples than in the control sample with no active coating layer.

After seven days of seeding, (SEM) images of cells on (HA1, TI1, SR1, and control), respectively, indicate the morphology of MC3T3-E1 cells on the samples Figure12. The cells' cytoplasmic extensions were evenly dispersed throughout all their surfaces. Over the nanofiber-coated surface of the (HA1) sample, the cells were aligned longitudinally with filopodia and cytoplasmic protrusions, as seen in Figure 12. a,b. TI1 Figure12.c,d and SR1 Figure12.e,f cells have a similar shape, both moderately polygonal or spherical and displaying prominently extended lamellipodia. The cells in the control sample Figure12 g, h are nearly round and distributed unevenly across the surface.

The SEM image, cell survival, and proliferation show that all samples were nontoxic to MC3T3-E1 cells and improved cell adhesion and proliferation. The variation in cell adhesion and proliferation across coated samples is related to the inclusion of distinct active nano ceramic particles, each with features that act together with the beneficial characteristics of the biopolymer and create a composite coating layer with multiple factions to enhance biocompatibility. The findings demonstrate that the electrospun composite coated layer facilitated excellent adherence and that its composition and morphology affected the cell adhesion behavior.
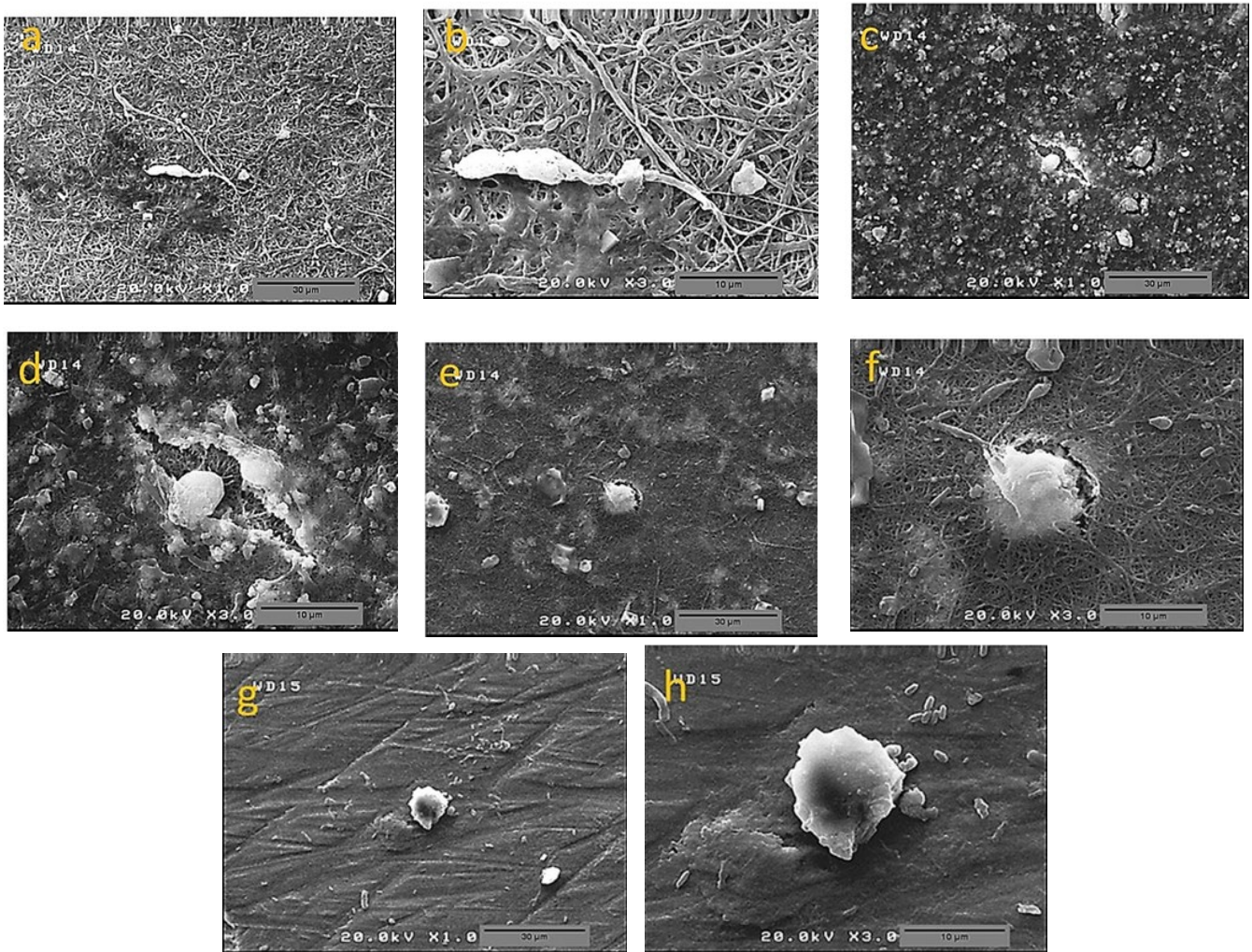
Figure 12: SEM images of MC3T3-E1 showing the morphology of cells on (a-b) HA1, (c-d) TI1, and (e-f) SR1,(g-h) bare Ti-25Zr, after seven days of cell seeding. [inset shows filopodial extensions formed on the material's surface

4. Conclusion

Powder metallurgy created Ti-25Zr alloy from elemental Ti and Zr powder. Ti-25Zr surface was functionalized by electrospinning nanocomposite fiber PCL/Chitosan with various nano-particles (nHA, nTiO2, nSrTiO3). This study examined coated and uncoated sample microstructure, mechanical, and biocompatibility. The following conclusion can be drawn:

1) Ti-25Zr alloy has a solid solution with α phase and superior mechanical properties than pure Ti, except for a 29% lower modulus of elasticity. Biomedical applications prefer this trait since it decreases stress shielding.
2) The electrospinning coating method produces nano-fiber with nano roughness, high surface contact area, and porosity, improving the positive reaction with the physiological medium and promoting cell adhesion and proliferation.
3) The water contact angle shows that all samples are hydrophilic, and the contact angle is lower for the coated surface than for the uncoated. hydrophilic surfaces can promote the initial phases of cell adhesion, differentiation, and proliferation, as well as bone mineralization
4) The antibacterial test shows no inhibition zone for the control sample (bare Ti-25Zr) alloy, while the coated samples show reasonable and comparable inhibition zone.
5) The addition of nano-particles (nHA,$nTiO_2$,$nSrTiO_3$) to the blend of PCL/Chitosan improved cell viability percentage in comparison with bare Ti-25Zr that have cell viability 80.52±1.97% at seven days, the coated samples significantly higher so (HA1) have 239.45±17.95%,(SR1) 170.09±8.12%, and (TI1) 117.19±19.42%.
6) Cell proliferation shows a significant increase with time for coated samples, and the enhancement reaches (197.76% HA1), (111.38% SR1), and (45.81 % TI1) in comparison with bare Ti-25Zr.
7) Cell morphology of coated samples shows the complete cover with spindle and polygon shape cells and extended cytoplasm over and around nano-fibers.

The study demonstrates that using electrospinning to create functional nano-fiber coatings on inert metal substrates effectively enhances osteoblast cell attachment, proliferation, and viability. The nanostructured surface improves cell-material interaction outcomes, making these materials suitable for orthodontic and orthopedic bone regeneration applications.

Acknowledgment

Author contribution

Conceptualization, E. Al-Hassani; A. Jabur; and A. Al-khateeb; methodology, A. Al-khateeb; validation, A. Al-khateeb; formal analysis, E. Al-Hassani and A. Jabur; investigation, A. Al-khateeb; resources, A. Al-khateeb; data curation, A. Al-khateeb; writing— A. Al-khateeb; writing—review and editing, S. Abu Bakar; supervision, E. Al-Hassani and A. Jabur. All authors have read and agreed to the published version of the manuscript.

Funding

Data availability statement

The data that support the findings of this study are available on request from the corresponding author.

Conflicts of interest

The authors declare that there is no conflict of interest.

References

[1] A. Das, V. Saxena, A. Bhardwaj, S. Rabha, L.M. Pandey, P. Dobbidi, Microstructural, interfacial, biological and electrical activity in sputtered Hydroxyapatite-Barium strontium titanate bilayered thin films, Surf. Interfaces, 31 (2022) 102063. https://doi.org/10.1016/j.surfin.2022.102063

[2] E. Al-Hassani, F. Al-Hassani, M. Najim, Effect of polymer coating on the osseointegration of CP-Ti dental implant, AIP Conf. Proc., 1968 (2018) 030022. https://doi.org/10.1063/1.5039209

[3] E.S. Al-Hassani, Effect of laser pulses on ion release behavior of Ti-base alloys, AIP Conf. Proc., 2190 (2019) 020030. https://doi.org/10.1063/1.5138516

[4] B. Wang, Z. Wu, J. Lan, Y. Li, L. Xie, X. Huang, A. Zhang, H. Qiao, X. Chang, H. Lin, H. Zhang, T. Li, Y. Huang, Surface modification of titanium implants by silk fibroin/Ag co-functionalized strontium titanate nanotubes for inhibition of bacterial-associated infection and enhancement of in vivo osseointegration, Surf. Coatings. Technol., 405 (2021) 126700. https://doi.org/10.1016/j.surfcoat.2020.126700

[5] C.M. Khashan, M. Khashan, A. Mutaib, Editor Notes and instructions, (2021) 26–27.

[6] S. Sahoo, A. Sinha, V. K. Balla, M. Das, Synthesis, characterization, and bioactivity of SrTiO3-incorporated titanium coating, J. Mater. Res., 33 (2018) 2087–2095. https://doi.org/10.1557/jmr.2018.99

[7] W. Zuo, L. Yu, J. Lin, Y. Yang, Q. Fei, Properties improvement of titanium alloys scaffolds in bone tissue engineering: a literature review, Ann. Transl. Med., 9 (2021) 1259. https://doi.org/10.21037/atm-20-8175

[8] E. S. Al-Hassani and F. J. Al-Hassani, Effect of Dual Surface Activation on the Surface Roughness of Titanium Dental Implant, Surface Treatments View project modules and bounded linear operators View project Effect of Dual Surface Activation on the Surface Roughness of Titanium Dental Implant,J. Nat. Sci. Res., Www.Iiste.Org ISSN. 7 (2017)35-44.

[9] X. Shen, W. Hu, L. Ping, C. Liu, L. Yao1, Z. Deng, G. Wu, Antibacterial and Osteogenic Functionalization of Titanium With Silicon/Copper-Doped High-Energy Shot Peening-Assisted Micro-Arc Oxidation Technique, 8 (2020). https://doi.org/10.3389/fbioe.2020.573464

[10] V. Alt, Antimicrobial coated implants in trauma and orthopaedics–A clinical review and risk-benefit analysis, 48 (2017) 599–607. https://doi.org/10.1016/j.injury.2016.12.011

[11] B. Wang, A. Bian, F. Jia, J. Lan, H. Yang, K. Yan, L. Xie, H. Qiao, X. Chang, H. Lin, H. Zhang, Y. Huang, Dual-functional strontium titanate nanotubes designed based on fusion peptides simultaneously enhancing anti-infection and osseointegration, Biomater. Adv., 133 (2022) 112650. https://doi.org/10.1016/j.msec.2022.112650

[12] S. Swain, C. Bowen, T. Rautray, Dual response of osteoblast activity and antibacterial properties of polarized strontium substituted hydroxyapatite—Barium strontium titanate composites with controlled strontium substitution, J. Biomed. Mater. Res. - Part A., 109 (2021) 2027–2035.

[13] E. Tranquillo, F. Bollino, Surface modifications for implants lifetime extension: An overview of sol-gel coatings, Coatings. 10 (2020) 589. https://doi.org/10.3390/COATINGS10060589

[14] A. R. Jabur, Antibacterial activity and heavy metal removal efficiency of electrospun medium molecular weight chitosan/nylon-6 nanofibre membranes, Biomed. Mater., 13 (2018) 015010 . https://doi.org/10.1088/1748-605X/aa9256

[15] T.Y. Jasim, M.A. Najim, A.R. Jabur, Improving the mechanical properties of (chitosan/polyurethane) electrospun blend scaffold used for skin regeneration, AIP Conf. Proc., 2123 (2019) 020042. https://doi.org/10.1063/1.5116969

[16] A.R. Jabur, E.S. Al-Hassani, A.M. Al-Shammari, M.A. Najim, A.A. Hassan, A.A. Ahmed, Evaluation of Stem Cells Growth on Electrospun Polycaprolactone (PCL) Scaffolds Used for Soft Tissue Applications, Energy Procedia, 119 (2017) 61–71. https://doi.org/10.1016/j.egypro.2017.07.048

[17] D. de Cassan, A. Becker, B. Glasmacher, Y. Roger, A. Hoffmann, T.R. Gengenbach, C.D. Easton, R. Hänsch, H. Menzel, Blending chitosan-g-poly(caprolactone) with poly(caprolactone) by electrospinning to produce functional fiber mats for tissue engineering applications, J. Appl. Polym. Sci., 137 (2020) 48650.

[18] F. Soleymani, R. Emadi, S. Sadeghzade, F. Tavangarian, Applying baghdadite/PCL/chitosan nanocomposite coating on AZ91 magnesium alloy to improve corrosion behavior, bioactivity, and biodegradability, Coatings. 9 (2019) 789. https://doi.org/10.3390/coatings9120789

[19] A. Al-Khateeb, E.S. Al-hassani, A.R. Jabur, Metallic Implant Surface Activation through Electrospinning Coating of Nanocomposite Fiber for Bone Regeneration, Int. J. Biomater., 2023 (2023) 1332814. https://doi.org/10.1155/2023/1332814

[20] B. Beig, U. Liaqat, M. Niazi, I. Douna, M. Zahoor, M. Niazi, Current challenges and innovative developments in hydroxyapatite-based coatings on metallic materials for bone implantation: A review, Coatings. 10 (2020) 1249. https://doi.org/10.3390/coatings10121249

[21] N. Nhlapo, T.C. Dzogbewu, O. Smidt, Nanofiber Polymers for Coating Titanium-Based Biomedical Implants, Fibers. 10 (2022) 36. https://doi.org/10.3390/fib10040036

[22] Y. Sun, H. Liu, X.Y. Sun, W. Xia, C. Deng, In vitro and in vivo study on the osseointegration of magnesium and strontium ion with two different proportions of mineralized collagen and its mechanism, J. Biomater. Appl., 36 (2021) 528–540.

[23] T. Tariverdian, A. Behnamghader, P. B. Milan, H. B. Bafrooei, M. Mozafari, 3D-printed barium strontium titanate-based piezoelectric scaffolds for bone tissue engineering, Ceram. Int., 45 (2019) 14029–14038. https://doi.org/10.1016/j.ceramint.2019.04.102

[24] A.R. Jabur, M.A. Najim, S.A.A. Al-Rahman, Study the effect of flow rate on some physical properties of different polymeric solutions, J. Phys. Conf. Ser., 1003 (2018) 012069. https://doi.org/10.1088/1742-6596/1003/1/012069

[25] B. Wang, W. Ruan, J. Liu, T. Zhang, H. Yang, J. Ruan, Microstructure, mechanical properties, and preliminary biocompatibility evaluation of binary Ti–Zr alloys for dental application, J. Biomater. Appl., 33 (2019) 766–775. https://doi.org/10.1177/0885328218811052

[26] M. Takahashi, M. Kikuchi, O. Okuno, Grindability of dental cast Ti-Zr alloys, Mater. Trans., 50 (2009) 859–863. https://doi.org/10.2320/matertrans.MRA2008403

[27] J. Jiang, C. Zhou, Y. Zhao, F. He, X. Wang, Development and properties of dental Ti–Zr binary alloys, J. Mech. Behav. Biomed. Mater., 112 (2020) 104048. https://doi.org/10.1016/j.jmbbm.2020.104048

[28] S. Zhang, L. Wang, Y. Bai, X. Lin, L. Peng, H. Chen, Experimental and theoretical analysis of a closed loop two-phase thermosiphon under various states for latent heat storage, Energy Reports. 6 (2020) 1–7. https://doi.org/10.1016/j.egyr.2019.09.005

[29] B. Yan, J. Tan, D. Wang, J. Qiu, X. Liu, Surface alloyed Ti–Zr layer constructed on titanium by Zr ion implantation for improving physicochemical and osteogenic properties, Prog. Nat. Sci. Mater. Int., 30 (2020) 635–641. https://doi.org/10.1016/j.pnsc.2020.09.006

[30] I. Matuła, G. Dercz, M. Zubko, J. Maszybrocka, J. J. Suliga, S. Golba, I. Jendrzejewska, Microstructure and porosity evolution of the ti–35zr biomedical alloy produced by elemental powder metallurgy, Mater., 13 (2020) 4539. https://doi.org/10.3390/ma13204539

[31] F.M. Ghorbani, B. Kaffashi, P. Shokrollahi, S. Akhlaghi, M.S. Hedenqvist, Effect of hydroxyapatite nano-particles on morphology, rheology and thermal behavior of poly(caprolactone)/chitosan blends, Mater. Sci. Eng. C ., 59 (2016) 980–989. https://doi.org/10.1016/j.msec.2015.10.076

[32] J. Yin, L. Xu, Batch preparation of electrospun polycaprolactone/chitosan/aloe vera blended nanofiber membranes for novel wound dressing, Int. J. Biol. Macromol., 160 (2020) 352–363. https://doi.org/10.1016/j.ijbiomac.2020.05.211

[33] E. Bolaina-Lorenzo, C. Martinez-Ramos, M. Monleón-Pradas, W. Herrera-Kao, J. V. Cauich-Rodriguez, J.M. Cervantes-Uc, Electrospun polycaprolactone/chitosan scaffolds for nerve tissue engineering: Physicochemical characterization and Schwann cell biocompatibility, Biomed. Mater. 12 (2016). https://doi.org/10.1088/1748-605x/12/1/015008

[34] H.C. Wu, J. Jiang, E.I. Meletis, Microstructure of BaCO3 and BaTiO3 coatings produced on titanium by plasma electrolytic oxidation, Appl. Surf. Sci., 506 (2020) 144858. https://doi.org/10.1016/j.apsusc.2019.144858

[35] M. Gazińska, A. Krokos, M. Kobielarz, M. Włodarczyk, P. Skibińska, B. Stępak, A. Antończak, M. Morawiak, P. Płociński, K. Rudnicka, Influence of hydroxyapatite surface functionalization on thermal and biological properties of poly(L-lactide)-and poly(l-lactide-co-glycolide)-based composites, Int. J. Mol. Sci., 21 (2020) 1–21. https://doi.org/10.3390/ijms21186711

[36] L.S. Chougala, M.S. Yatnatti, R.K. Linganagoudar, R.R. Kamble, J.S. Kadadevarmath, A simple approach on synthesis of TiO2 nanoparticles and its application in dye sensitized solar cells, J. Nano- Electron. Phys., 9 (2017) 04005. https://doi.org/10.21272/jnep.9(4).04005.

[37] M.S. Hanafy, W.M. Desoky, E.M. Hussein, N.H. El-Shaer, M. Gomaa, A.A. Gamal, M.A. Esawy, O.W. Guirguis, Biological applications study of bio-nanocomposites based on chitosan/TiO2 nanoparticles polymeric films modified by oleic acid, J. Biomed. Mater. Res. - Part A. 109 (2021) 232–247. https://doi.org/10.1002/jbm.a.37019

[38] L.M. Anaya-Esparza, J.M. Ruvalcaba-Gómez, C.I. Maytorena-Verdugo, N. González-Silva, R. Romero-Toledo, S. Aguilera-Aguirre, A. Pérez-Larios, E. Montalvo-González, Chitosan-tio2: A versatile hybrid composite, Materials (Basel). 13 (2020) 811. https://doi.org/10.3390/ma13040811

[39] M. Prodana, C.E. Nistor, A.B. Stoian, D. Ionita, C. Burnei, Dual nanofibrous bioactive coatings on TiZr implants, Coatings. 10 (2020) 526. https://doi.org/10.3390/COATINGS10060526

[40] G. Li, Q. Xiao, R. McNaughton, L. Han, L. Zhang, Y. Wang, Y. Yang, Nanoengineered porous chitosan/CaTiO3 hybrid scaffolds for accelerating Schwann cells growth in peripheral nerve regeneration, Colloids Surf. B Biointerfaces, 158 (2017) 57–67. https://doi.org/10.1016/j.colsurfb.2017.06.026

[41] R.M. Jin, N. Sultana, S. Baba, S. Hamdan, A.F. Ismail, Porous PCL/Chitosan and nHA/PCL/chitosan scaffolds for tissue engineering applications: Fabrication and evaluation, J. Nanomater. 2015 (2015). https://doi.org/10.1155/2015/357372

[42] L. Zhu, W. Gu, H. Li, W. Zou, H. Liu, Y. Zhang, Q. Wu, Z. Fu, Y. Lu, Enhancing the photocatalytic hydrogen production performance of SrTiO3 by coating with a hydrophilic poloxamer, Appl. Surf. Sci., 528 (2020) 146837. https://doi.org/10.1016/j.apsusc.2020.146837

[43] H. Qiao, Q. Zou, C. Yuan, X. Zhang, S. Han, Z. Wang, X. Bu, H. Tang, Y. Huang, Composite coatings of lanthanum-doped fluor-hydroxyapatite and a layer of strontium titanate nanotubes: fabrication, bio-corrosion resistance, cytocompatibility and osteogenic differentiation, Ceram. Int., 44 (2018) 16632–16646. https://doi.org/10.1016/j.ceramint.2018.06.090

[44] B. Kolathupalayam Shanmugam, S. Rangaraj, K. Subramani, S. Srinivasan, W.K. Aicher, R. Venkatachalam, Biomimetic TiO2-chitosan/sodium alginate blended nanocomposite scaffolds for tissue engineering applications, Mater. Sci. Eng. C., 110 (2020) 110710. https://doi.org/10.1016/j.msec.2020.110710

[45] M.M. Farag, W.M. Abd-Allah, H.Y.A. Ahmed, Study of the dual effect of gamma irradiation and strontium substitution on bioactivity, cytotoxicity, and antimicrobial properties of 45S5 bioglass, J. Biomed. Mater. Res. - Part A. 105 (2017) 1646–1655. https://doi.org/10.1002/jbm.a.36035

[46] X. Ge, C. Ren, Y. Ding, G. Chen, X. Lu, K. Wang, F. Ren, M. Yang, Z. Wang, J. Li, X. An, B. Qian, Y. Leng, Micro/nano-structured TiO2 surface with dual-functional antibacterial effects for biomedical applications, Bioact. Mater., 4 (2019) 346–357. https://doi.org/10.1016/j.bioactmat.2019.10.006

[47] P.L. Hariani, M. Muryati, M. Said, S. Salni, Synthesis of nano-hydroxyapatite from snakehead (Channa striata) fish bone and its antibacterial properties, Key Eng. Mater., 840 (2020) 293–299. https://doi.org/10.4028/www.scientific.net/kem.840.293

[48] L. Chen, S. Al-Bayatee, Z. Khurshid, A. Shavandi, P. Brunton, J. Ratnayake, Hydroxyapatite in oral care products—a review, Materials (Basel). 14 (2021) 4865. https://doi.org/10.3390/ma14174865

[49] H. Chang, H. Xiang, Z. Yao, S. Yang, M. Tu, X. Zhang, B. Yu, Strontium-substituted calcium sulfate hemihydrate/hydroxyapatite scaffold enhances bone regeneration by recruiting bone mesenchymal stromal cells, J. Biomater. Appl., 35 (2020) 97–107. https://doi.org/10.1177/0885328220915816

[50] L. Zhao, T. Liu, X. Li, Q. Cui, X. Wang, K. Song, D. Ge, Protein adsorption on TiO2 nanostructures and its effects on surface topography and bactericidal performance, Appl. Surf. Sci., 576 (2022) 151779. https://doi.org/10.1016/j.apsusc.2021.151779